The Journal of Clinical Investigation

Lymphatic dysfunction in lupus contributes to cutaneous photosensitivity and lymph node B cell responses

Mir J. Howlader, William G. Ambler, Madhavi Latha S. Chalasani, Aahna Rathod, Ethan S. Seltzer, Ji Hyun Sim, Jinyeon Shin, Noa Schwartz, William D. Shipman III, Dragos C. Dasoveanu, Camila B. Carballo, Ecem Sevim, Salma Siddique, Yurii Chinenov, Scott A. Rodeo, Doruk Erkan, Raghu P. Kataru, Babak J. Mehrara, Theresa T. Lu

J Clin Invest. 2025;135(12):e168412. https://doi.org/10.1172/JCI168412.

Research Article Autoimmunity Immunology Inflammation Vascular biology

Graphical abstract

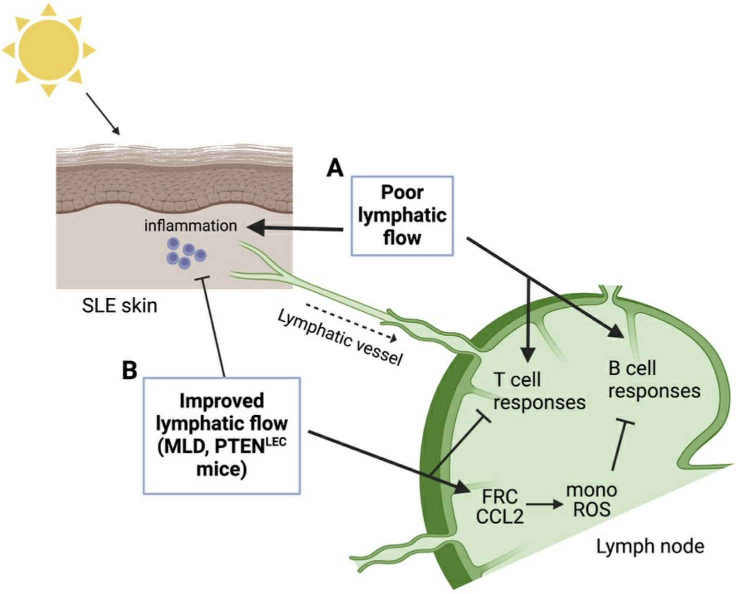

The Journal of Clinical Investigation

Lymphatic dysfunction in lupus contributes to cutaneous photosensitivity and lymph node B cell responses

Mir J. Howlader,[1,2] William G. Ambler,[1,3] Madhavi Latha S. Chalasani,[1,4] Aahna Rathod,[1] Ethan S. Seltzer,[1] Ji Hyun Sim,[1,4] Jinyeon Shin,[5] Noa Schwartz,[1,6] William D. Shipman III,[1,7,8] Dragos C. Dasoveanu,[1,9] Camila B. Carballo,[10] Ecem Sevim,[6] Salma Siddique,[3,6] Yurii Chinenov,[11] Scott A. Rodeo,[10,12] Doruk Erkan,[6] Raghu P. Kataru,[5] Babak J. Mehrara,[5] and Theresa T. Lu[1,3,4,6,8]

[1]Autoimmunity and Inflammation Program, Hospital for Special Surgery Research Institute, New York, New York, USA. [2]Biochemistry, Structural Biology, Cell Biology, Developmental Biology and Molecular Biology Graduate Program, Weill Cornell Medicine, New York, New York, USA. [3]Pediatric Rheumatology, Department of Medicine, Hospital for Special Surgery, New York, New York, USA. [4]Department of Microbiology and Immunology, Weill Cornell Medicine, New York, New York, USA. [5]Division of Plastic and Reconstructive Surgery, Department of Surgery, Memorial Sloan Kettering Cancer Center, New York, New York, USA. [6]Rheumatology, Department of Medicine, Hospital for Special Surgery, New York, New York, USA. [7]Weill Cornell/Rockefeller/Sloan-Kettering Tri-Institutional MD-PhD Program, New York, New York, USA. [8]Immunology and Microbial Pathogenesis Graduate Program and [9]Physiology, Biophysics, and Systems Biology Graduate Program, Weill Cornell Medicine, New York, New York, USA. [10]Orthopedic Soft Tissue Research Program, Hospital for Special Surgery Research Institute, New York, New York, USA. [11]David Z. Rosenweig Genomics Research Center, Hospital for Special Surgery Research Institute, New York, New York, USA. [12]Department of Orthopedics, Hospital for Special Surgery, New York, New York, USA.

Patients with systemic lupus erythematosus (SLE) are photosensitive, developing skin inflammation with even ambient ultraviolet radiation (UVR), and this cutaneous photosensitivity can be associated with UVR-induced flares of systemic disease, which can involve increased autoantibodies and further end-organ injury. Mechanistic insight into the link between the skin responses and autoimmunity is limited. Signals from skin are transmitted directly to the immune system via lymphatic vessels, and here we show evidence for potentiation of UVR-induced lymphatic flow dysfunction in SLE patients and murine models. Improving lymphatic flow by manual lymphatic drainage (MLD) or with a transgenic model with increased lymphatic vessels reduces both cutaneous inflammation and lymph node B and T cell responses, and long-term MLD reduces splenomegaly and titers of a number of autoantibodies. Mechanistically, improved flow restrains B cell responses in part by stimulating a lymph node fibroblastic reticular cell-monocyte axis. Our results point to lymphatic modulation of lymph node stromal function as a link between photosensitive skin responses and autoimmunity and as a therapeutic target in lupus, provide insight into mechanisms by which the skin state regulates draining lymph node function, and suggest the possibility of MLD as an accessible and cost-effective adjunct to add to ongoing medical therapies for lupus and related diseases.

Introduction

Photosensitivity, a cutaneous sensitivity to ultraviolet radiation (UVR), affects the majority of systemic lupus erythematosus (SLE) patients, but, in addition to inflammatory skin lesions, UVR exposure can trigger systemic disease flares in both patients and murine models that can include increased autoantibody levels and further end-organ injury (1–5). Currently, medications used for photosensitive skin responses include topical steroids, topical calcineurin inhibitors, and antimalarials such as hydroxychloroquine. More importantly, lupus patients are advised to reduce UVR exposure by avoiding the sun, wearing protective clothing, and wearing sunscreen to prevent photosensitive skin responses and their sequelae (6–8). Photosensitive skin inflammation, the accompanying risk of systemic disease flares, and the lifestyle modifications needed to prevent these all contribute to disrupting patients' quality of life (9–11). Advances have begun to delineate the mechanisms that contribute to photosensitivity (12–14). However, the link between UVR-induced skin inflammation and increased autoantibody titers in these photosensitive patients remains poorly understood.

Skin communicates with lymphoid tissues via lymphatic vessels that transport cells and interstitial fluid to skin-draining lymph nodes where immune responses occur and can be regulated. This lymphatic transport serves both to clear fluid and inflammation from the skin and to deliver antigens, antigen-presenting cells, and mediators that impact lymph node function (15, 16). Reduced lymphatic flow results in exacerbated skin inflammation and, over time, can lead to the development of autoantibodies (17, 18). This latter scenario is not well understood mechanistically, but the combination of skin inflammation and autoimmunity is reminiscent of SLE and raises the possibility of lymphatic dysfunction in SLE, which has been described anecdotally (19–22).

Lymphatic flow brings both dendritic cells and lymph fluid to the subcapsular sinus of the draining lymph node, at which point they take divergent paths. Dendritic cells migrating from the skin

---

Authorship note: MJH and WGA are co–first authors.

Conflict of interest: The authors have declared that no conflict of interest exists.

Submitted: December 28, 2022; **Accepted:** April 11, 2025; **Published:** April 22, 2025.
Reference information: *J Clin Invest*. 2025;135(12):e168412.
https://doi.org/10.1172/JCI168412.

actively leave the sinus to enter the nodal parenchyma where T and B cells are located (23). Lymph fluid containing soluble molecules, on the other hand, flows into the conduit system (24). The conduits consist of a central collagen core ensheathed by fibroblastic reticular cells (FRCs), and the potential space between the collagen core and the FRCs allows for flow of lymph fluid throughout the lymph node until the lymph leaves the node mainly via efferent lymphatic flow. Comprising the wall of the conduit system then, FRCs are among the major first sensors of signals flowing from the skin. FRCs, in turn, play critical roles regulating T and B cell responses (25–27), and we recently showed that immunization of healthy mice upregulated FRC-derived CCL2, which promoted CCR2$^+$Ly6C$^+$ monocyte expression of ROS to limit plasmablast survival (28). Lymphatic input from skin to lymph nodes that alters FRC phenotype then could potentially affect lymph node B cell responses.

In this study, we examined for lymphatic dysfunction in both human SLE and murine SLE models and sought to understand the consequences on both skin and lymph node function. We show evidence for potentiation of UVR-induced flow dysfunction in human SLE and in multiple photosensitive SLE models. Improving lymphatic flow by manual lymphatic drainage (MLD) or with a transgenic model with increased lymphatic flow reduced UVR-induced skin inflammation, draining lymph node B and T cell responses, and MLD over a prolonged period of time reduced splenomegaly and titers of a number of autoantibodies. We further show that improving lymphatic flow upregulates FRC CCL2, and that depleting monocytes limits the flow-induced reduction in plasmablasts. These results suggest that SLE skin is primed for UVR-induced lymphatic flow dysfunction, and the dysfunction contributes to both cutaneous photosensitive responses and, by modulating a FRC-monocyte axis, lymph node B cell activity in disease. This scenario suggests that improving lymphatic flow and its consequences on the lymph node stromal microenvironment may be therapeutically useful in SLE.

Results

Evidence of dysfunctional dermal lymph flow in SLE patients and mouse models. We assessed for evidence of lymphatic flow alterations in the skin of SLE patients and SLE mouse models. In human skin, greater lumenal area of lymphatic vessels can be reflective of distention from reduced lymphatic flow (29–31). We examined biopsies that we had previously obtained from the sun-exposed forearm skin of patients with SLE and with persistently positive antiphospholipid antibodies (APL), a condition that can overlap with SLE. These biopsies were taken from sites of livedo reticularis, a lacy pattern of prominent veins on otherwise normal-appearing skin that is not considered to be related to photosensitivity and that affects both SLE and APL patients (32). We compared the samples from SLE patients (some of whom also had APL) to that of APL patients without SLE. SLE skin showed dilated lymphatic vessels when compared with APL-only skin (Figure 1, A and B). There was no change in the density of lymphatic vessels (Figure 1C). While these results are in the context of livedo skin, the differences between SLE and non-SLE patients suggested that there is dysfunctional lymphatic flow in human SLE skin that is exposed to UVR.

We examined lymphatic flow in lupus model mice by assaying for retention in the skin of intradermally injected Evans blue dye (33) after UVR treatment. We focused on ear skin as it has little fur, allowing the skin to be directly exposed to UVR. We used 2 photosensitive lupus models, the MRL-*Fas*^{lpr} (LPR) spontaneous lupus model (34–36) and the imiquimod (IMQ) lupus model that is induced by chronic epicutaneous IMQ application (37). The LPR mice and their MRL-MpJ (MRL) controls were treated with 1000J UVB/m2/day of UVR for 4 days prior to Evans blue dye injection in the ear skin (Figure 1D). LPR mice showed increased Evans blue dye retention in the ear when compared with MRL mice (Figure 1E), suggesting reduced flow out of the ear skin. As expected for the photosensitive LPR mice, there was greater UVR-induced skin swelling in LPR mice when compared with control MRL mice (Figure 1F). The greater Evans blue dye retention in LPR mice was specific to UVR exposure, as LPR mice showed no increases in Evans blue dye retention or ear thickness at baseline without UVR (Figure 1, G and H).

The UVR-induced lymphatic alterations and ear swelling were accompanied by the accumulation of inflammatory cells. We had previously shown that inflammatory Ly6C^{hi} monocytes accumulated after 1 day of UVR in LPR mice (35). After 4 days of UVR, monocyte numbers accumulated in greater numbers in both MRL and LPR mice treated with UVR at comparable levels (Figure 1I). However, TCRαβ$^+$ CD4 T cells and TCRαβ$^+$CD3$^+$CD4$^-$CD8$^-$ "double negative" (DN) T cells that are characteristic of LPR mice (38) both accumulated in greater numbers in LPR mice compared with MRL mice at this time point (Figure 1, J and K). Neutrophils, CD8$^+$ T cells, and TCRγδ T cells showed no changes between LPR and MRL mice (Supplemental Figure 1, A–C; supplemental material available online with this article; https://doi.org/10.1172/JCI168412DS1). Together with the Evans blue dye experiments, these results indicated that lymphatic flow dysfunction accompanies the increased inflammation in the skin (as indicated by the greater edema and T cell infiltrate) in UVR-treated LPR mice. These results suggested the possibility that lymphatic flow dysfunction, by failing to remove fluid and inflammatory mediators from the skin, was contributing to the increased skin inflammation of the lupus model mice.

We examined the IMQ model (37), inducing this model in B6 mice by applying IMQ, a TLR7 agonist, to the skin for 4–5 weeks, yielding B6-IMQ mice (Figure 1L). IMQ was applied on the right ear only, and the skin on the rest of the body, including the left ear, was considered "nonlesional" skin and reflective of systemic disease. We have shown previously that the nonlesional left ear in IMQ mice is similar to nonlesional skin in human lupus in expressing an IFN signature, whereas the right ear has a less robust IFN signature (39). Additionally, the right ear, even without UVR exposure, showed upregulation of apoptotic pathways (Supplemental Figure 2A), suggesting that there was tissue damage from repeated local treatment of IMQ. To assess effects of UVR exposure without confounding results from direct IMQ treatment, we focused on the left, nonlesional ear. The left ear showed increased Evans blue dye retention with increased skin swelling upon UVR exposure when compared with vehicle-painted controls (Figure 1, M and N). Similarly, the footpad of B6-IMQ mice showed increased Evans blue dye retention when compared with B6 mice (Figure 1O), suggesting that the dermal lymphatic dysfunction in B6-IMQ mice affected nonlesional skin throughout the body and that the left ear results were not reflective of direct exposure to IMQ that had transferred from the right ear. The right

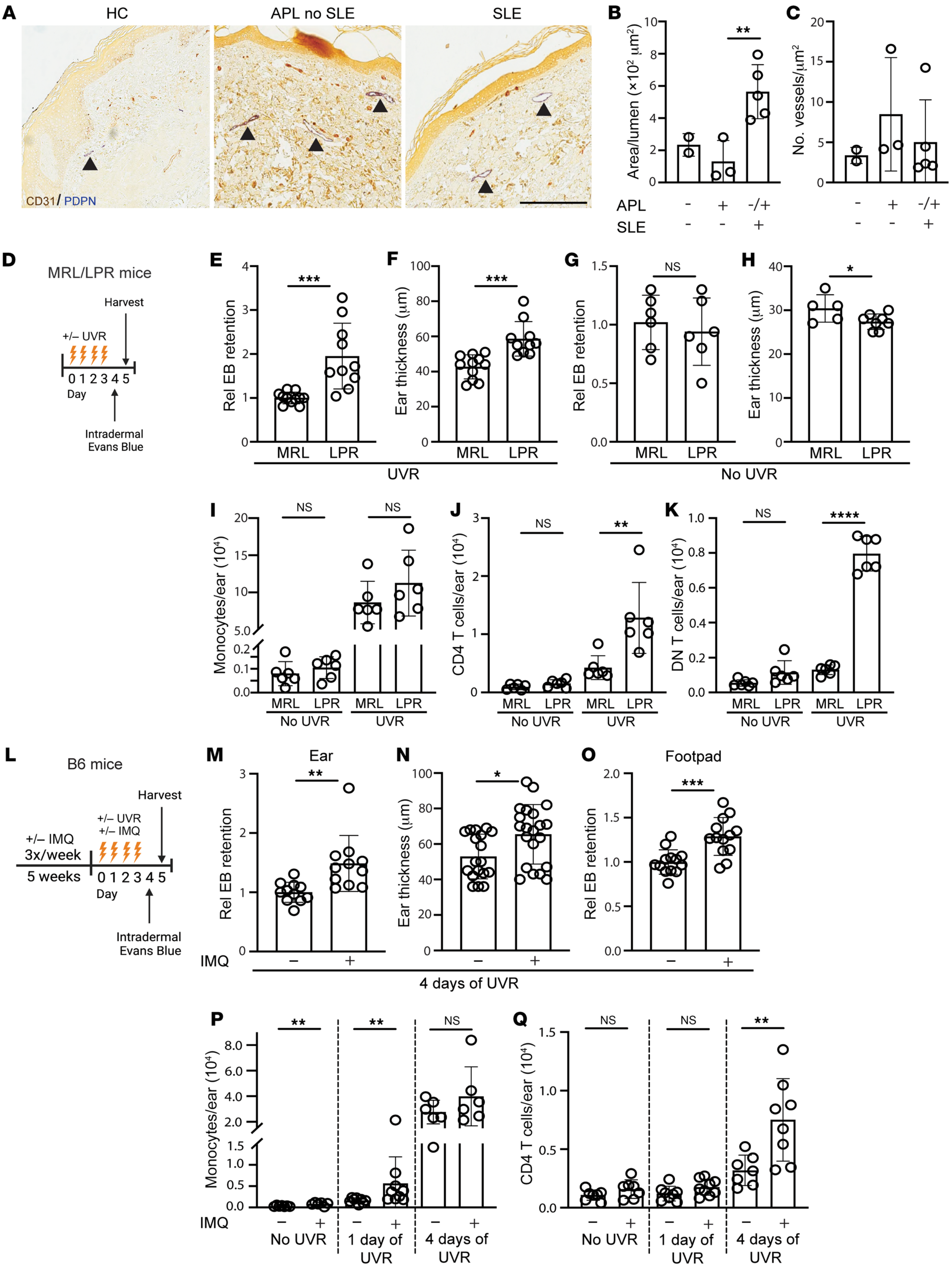
A
HC
APL no SLE
SLE
CD31/ PDPN
B
Area/lumen (×10² µm²)
**
APL - + -/+
SLE - - +
C
No. vessels/µm²
D
MRL/LPR mice
Harvest
+/– UVR
0 1 2 3 4 5
Day
Intradermal Evans Blue
E
Rel EB retention
***
F
Ear thickness (µm)
***
G
NS
H
*
MRL LPR
UVR
No UVR
I
Monocytes/ear (10⁴)
NS
J
CD4 T cells/ear (10⁴)
**
K
DN T cells/ear (10⁴)
****
L
B6 mice
+/– IMQ 3x/week
5 weeks
+/– UVR +/– IMQ
M
Ear
N
O
Footpad
IMQ – +
4 days of UVR
P
Q
No UVR
1 day of UVR
4 days of UVR

Figure 1. Patients with SLE and murine SLE models show evidence of cutaneous lymphatic dysfunction. (**A**–**C**) Punch biopsies of forearm skin from healthy control (HC), positive APLs without SLE, and SLE subjects with or without APL were stained for CD31$^+$PDPN$^+$ lymphatic vessels. (**A**) Representative photomicrographs. Arrowheads point to lymphatic vessels. Original magnification ×40. (**B**) Lumenal area per vessel. Each symbol is an individual subject. (**C**) Number of lymphatic vessels per tissue area. (**D**–**H**) LPR mice and MRL controls were treated with UVR for 4 consecutive days, injected in ear pinna with Evans blue dye (EB) 1 day after final UVR dose, and ear harvested to assess EB content 1 day later, as in **D**. (**E**) EB retention and (**F**) ear swelling was quantified after UVR or (**G** and **H**) with no UVR. (**I**–**K**) Ears were examined by flow cytometry at 24 hours after final dose of UVR. (**I**) Monocyte, (**J**) TCR CD4$^+$ T cell, and (**K**) TCRab$^+$CD3$^+$ CD4$^-$CD8$^-$ DN T cell numbers. (**L**–**O**) B6 mice received IMQ on the right ear and were exposed to UVR, and EB retention after intradermal injection of left ear or footpad was compared with responses in vehicle-treated control mice, as in **L**. (**M**) EB retention in ear. (**N**) Ear swelling. (**O**) EB retention in footpad. (**P** and **Q**) Left ear was collected 24 hours after 1 or 4 doses of UVR. (**P**) Monocyte and (**Q**) TCR CD4$^+$ T cell numbers. Each symbol represents 1 mouse; $n = 2$ to 21 per condition; data are from 2 (**I**–**K**), 3 (**M** and **O**), 4 (**G** and **H**), 6 (**E** and **F**), 10 (**N**), and 11 (**P** and **Q**) independent experiments. Normality was assessed using the Shapiro-Wilk test. If normal, unpaired *t* test was used. If data were not normal, Mann-Whitney *U* test was used. $^{***}P < 0.001$; $^{**}P < 0.01$; $^{*}P < 0.05$. Error bars represent SD.

ear also showed increased Evans blue dye retention and increased ear thickness (Supplemental Figure 2, B and C).

Characterization of the inflammatory infiltrate in B6-IMQ mice showed a higher baseline monocyte number in B6-IMQ compared with B6 mice, and UVR exposure for 1 day showed greater monocyte accumulation in B6-IMQ mice (Figure 1P). Monocyte accumulation continued to increase with additional days of UVR exposure, and monocytes were equally high in B6-IMQ and B6 ears after 4 days of UVR (Figure 1P). In contrast, CD4$^+$ T cell number accumulation was limited until after 4 days of UVR, when B6-IMQ showed higher numbers of CD4$^+$ T cells than B6 mice (Figure 1Q). Neutrophils, TCRαβ CD8$^+$ T cells, and TCRγδ T cells showed no changes between IMQ and control mice after 4 days of UVR exposure (Supplemental Figure 1, D–F). Similar to LPR mice then, B6-IMQ mice showed that UVR-induced skin inflammation after 4 days of treatment included lymphatic dysfunction along with tissue swelling and T cell accumulation. Together, our findings in 2 distinct SLE models suggested that photosensitive skin is characterized in part by UVR-induced lymphatic dysfunction, supporting the evidence of lymphatic dysfunction in sun-exposed skin in human SLE.

Improving lymphatic flow reduces photosensitivity of skin in SLE models. We asked about the contribution of reduced lymphatic flow to cutaneous photosensitive responses in the SLE models by using 2 different approaches to improve lymphatic flow. One approach was through MLD, a technique used by physical therapists to reduce swelling in patients with acquired or congenital lymphedema (40, 41). We administered MLD targeting the left ear once a day during the course of UVR exposure (Figure 2, A and B). This treatment decreased Evans blue retention in LPR mice relative to handling controls (Figure 2C and Supplemental Figure 3A), suggesting that MLD was successful in improving lymphatic flow. MLD also ameliorated UVR-induced skin inflammation, with reductions in ear swelling (Figure 2, D and E), CD4$^+$ T cell numbers, and IFN-γ expression (Figure 2, F–H), and DN T cell numbers and IFN-γ expression (Figure 2, I and J). The proportion of Tregs and Th17 cells within the CD4$^+$ T cell population, the proportion of IL-17–expressing DN cells, and the number of CD8$^+$ T cells did not change with MLD (Supplemental Figure 3, B–E). Monocyte and neutrophil numbers also remained unchanged (Supplemental Figure 3, F and G). These results suggested that improving lymphatic flow with MLD was able to both reduce ear swelling and T cell accumulation and activity in UVR-treated LPR mice.

MLD had similar effects in B6-IMQ mice (Figure 2, K–P). Evans blue dye retention was reduced (Figure 2L), suggesting improved lymphatic flow, and this was accompanied by reduced ear swelling (Figure 2M). Both total CD4$^+$ T cell numbers and IFN-γ–expressing Th1 proportion were also decreased with MLD (Figure 2, N–P). Similar to LPR mice, MLD had no effect on Treg, Th17, CD8$^+$ T cell, monocyte, or neutrophil accumulation (Supplemental Figure 3, H–L). Our results together suggested that improving lymphatic flow with MLD ameliorated UVR-induced cutaneous inflammation in both the LPR and IMQ SLE models.

Our second approach to improving lymph flow was by using transgenic Flt4Cre^{ERT2}PTEN$^{fl/fl}$ mice (42). When treated with tamoxifen, these mice have lymphatic endothelial cell–specific (LEC-specific) deletion of phosphatase and tensin homolog (PTEN), an antagonist of critical VEGFC/VEGFR3 signaling. This results in expansion of functional lymphatic vessels, improved lymphatic flow from skin, and reduced UVR-induced skin inflammation in healthy (i.e., nonlupus) mice (42). We confirmed that tamoxifen treatment of Flt4Cre^{ERT2}PTEN$^{fl/fl}$ mice specifically deleted PTEN from LECs (Supplemental Figure 4A). We designated the tamoxifen-treated mice as LEC^{PTEN} mice and non–tamoxifen-treated mice as LEC^{WT} mice and induced the IMQ model in them to generate LEC^{PTEN}-IMQ and LEC^{WT}-IMQ mice (Figure 2Q). Reduced Evans blue dye retention in the left ear of LEC^{PTEN}-IMQ mice compared with LEC^{WT}-IMQ controls confirmed improved lymphatic drainage (Figure 2R), and this was associated with reduced UVR-induced ear swelling (Figure 2S), suggesting that improving lymphatic flow reduced the ear swelling. Similar to MLD, the genetic approach to improving lymphatic flow reduced CD4$^+$ T cell numbers in LEC^{PTEN}-IMQ mice compared with LEC^{WT}-IMQ mice (Figure 2, T and U). Notably, tamoxifen treatment of nontransgenic B6 mice did not reduce Evans blue dye retention or ear swelling (Figure 2, V and W), suggesting that effects in LEC^{PTEN}-IMQ mice were attributable to PTEN deletion rather than to tamoxifen treatment. Treg, CD8$^+$ T cell, monocyte, and neutrophil numbers remained unchanged (Supplemental Figure 3, M–P). The right ear of LEC^{PTEN}-IMQ mice also showed reduced Evans blue dye retention and ear swelling when compared with LEC^{WT}-IMQ mice and no changes in monocyte and neutrophil numbers (Supplemental Figure 4, B–E). As with the left ear, B6-IMQ mice showed no reduction in Evans blue dye retention or ear thickness with tamoxifen (Supplemental Figure 4, F and G). Consistent with prior reports that improved lymphatic drainage can reduce cutaneous inflammation (33, 42, 43), our results from using both an acute physical approach in 2 lupus models and a long-term genetic approach showed that improving lymphatic flow from skin reduces cutaneous UVR-induced inflammation in SLE model mice, suggesting that the lymphatic dysfunction contributes to photosensitive skin responses in SLE.

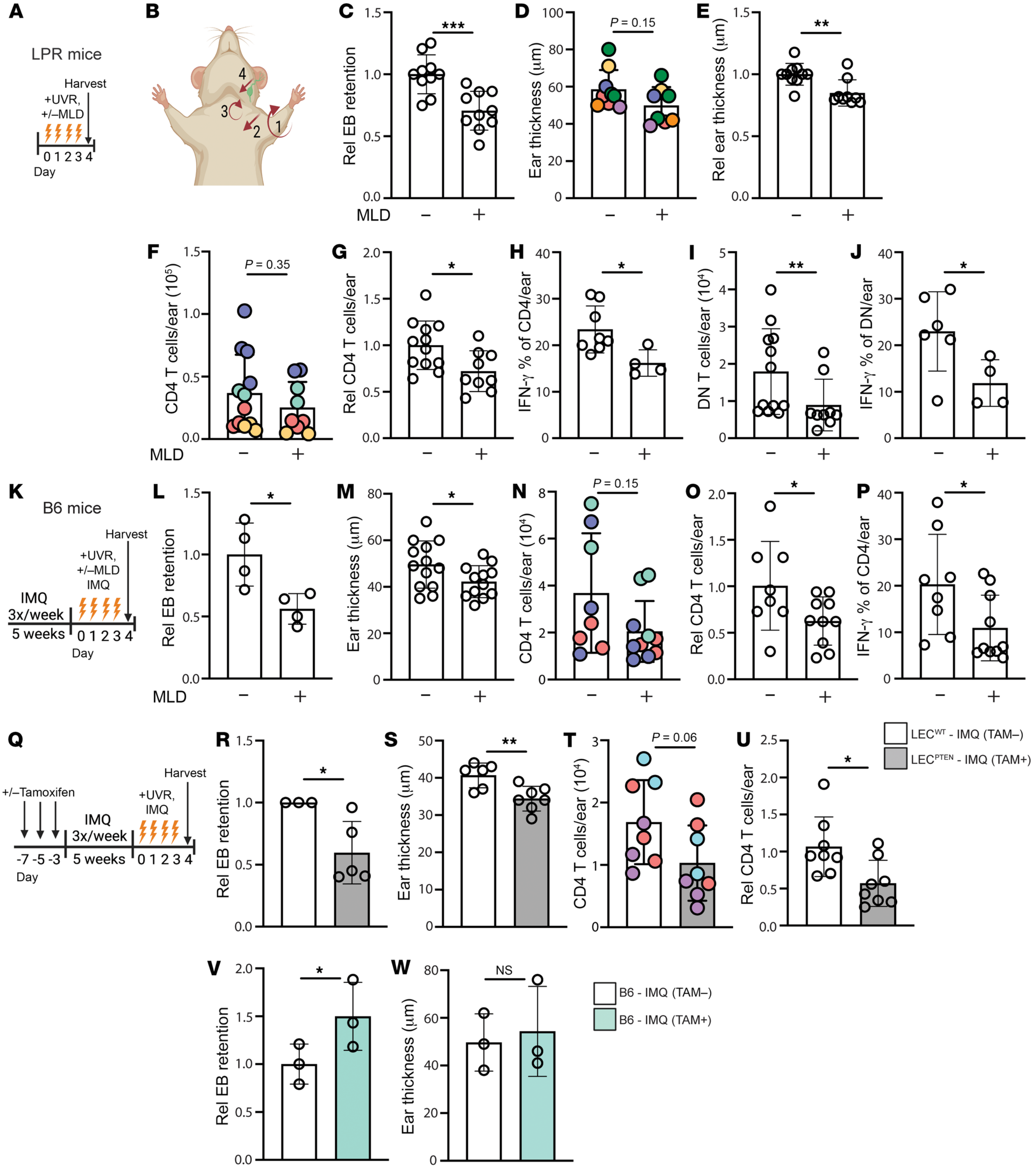

Figure 2. Improving lymphatic flow reduces cutaneous photosensitive responses in SLE models. (**A**–**J**) LPR mice and (**K**–**P**) B6-IMQ mice were treated with UVR and MLD targeting the left ear or were control handled. Left ear was then examined. (**A** and **K**) Experimental design. (**B**) Illustration of MLD technique. Please see Methods for details. (**C** and **L**) EB retention and (**D**, **E**, and **M**) ear thickness, absolute (**D** and **M**) or normalized (**E**). (**F** and **N**) TCR CD4$^+$ T cell numbers, (**G** and **O**) normalized to controls. (**H** and **P**) Percentage of CD4$^+$ T cells that express IFN-γ. (**I**) DN T cell numbers and (**J**) percentage that express IFN-γ. (**Q**–**U**) Flt4Cre^{ERT2} PTEN$^{fl/fl}$ mice treated with tamoxifen (LEC^{PTEN}) or without (LEC^{WT}) were treated with IMQ on right ear and UVR before left ear skin assessment, as in **Q**. (**R**) EB retention, (**S**) skin thickness, (**T**) TCR CD4$^+$ T cell numbers, and (**U**) IFN-γ$^+$ percentage. (**V** and **W**) Nontransgenic B6 mice were treated as described in **Q**. (**V**) EB retention and (**W**) ear thickness. Each symbol represents 1 mouse; $n = 3$ to 13 per condition; data are from 2 (**H**, **J**, **L**, **V**, and **W**), 3 (**N**, **O**, **P**, **R**, **T**, and **U**), 4 (**F**, **G**, **I**, and **S**), 6 (**C**), 7 (**D** and **E**), and 9 (**M**) independent experiments. Normality was assessed using the Shapiro-Wilk test. If normal, unpaired *t* test was used. If data were not normal, Mann-Whitney *U* test was used. ***$P < 0.001$; **$P < 0.01$; *$P < 0.05$. Error bars represent SD.

Improving lymphatic flow reduces draining lymph node B cell responses in SLE models. We asked whether lymphatic flow alterations in SLE models contributed to modulating immune activity in downstream lymph nodes. Improving lymphatic flow with MLD over 4 days in LPR mice during UVR exposure did not affect overall lymph node cellularity or overall B cell numbers in draining auricular nodes (Figure 3, A and B), but did reduce germinal center B cell and plasmablast numbers (Figure 3, C and D). $CD4^+$ T cell numbers were also reduced (Figure 3, E and F), as was the frequency of T follicular helper (TFH) cells (Supplemental Figure 5A), which could have contributed to reduced germinal center B cell responses. Th1 (Figure 3G), Treg, and Th17 frequencies were unchanged (Supplemental Figure 5, B and C). $CD8^+$ (Figure 3H), and DN T cell (Figure 3I) numbers were unchanged, as was the expression of IL-17 by DN cells (Supplemental Figure 5D). These data suggested that improving lymphatic flow with MLD in LPR mice reduces draining lymph node germinal center and plasmablast responses along with overall $CD4^+$ T cell numbers and the proportion of TFH cells.

Similar to LPR mice, MLD in B6-IMQ mice showed no effects on total lymph node (LN) cellularity or on overall B cells (Figure 3, J and K), but did reduce germinal center B cell, plasmablast, and $CD4^+$ T cell numbers (Figure 3, L–O). Note that the reduction in germinal center (2.2-fold) and plasmablast (2.4-fold) numbers reflects a partial reduction rather than normalization to a nonlupus state, as UVR-treated B6 mice have very few germinal center cells and plasmablasts (1002+/–859 and 312+/–220 per lymph node, respectively). Unlike in LPR mice, MLD in B6-IMQ mice did not reduce TFH cells (Supplemental Figure 5E) but did reduce Th1 frequency (Figure 3P). Tregs and Th17 cell frequencies (Supplemental Figure 5, F and G) and $CD8^+$ T cell numbers (Figure 3Q) were unchanged. These data together showed that MLD in LPR and IMQ models reduced B cell responses and $CD4^+$ T cell numbers and differentiation, thus suggesting that even a short period of improved lymphatic flow from skin can reduce B and $CD4^+$ T cell responses.

In contrast to LPR and B6-IMQ mice treated with MLD, LEC^{PTEN}-IMQ mice showed decreases in lymph node cellularity and overall B cells when compared with LEC^{WT}-IMQ mice (Figure 3, R and S). As with LPR and B6-IMQ mice, germinal center B cell, plasmablast, and $CD4^+$ T cell numbers were reduced (Figure 3, T–W). Th1 (Figure 3X), TFH, and Treg frequencies (Supplemental Figure 5, H and I) and $CD8^+$ T cell numbers (Figure 3Y) were unchanged. These data suggest that improving lymph flow genetically and before induction of lupus disease activity reduced overall lymph node cellularity and, similarly to short-term MLD, preferentially reduced B cell and CD4 responses.

Longer duration of improved lymphatic flow reduces systemic disease activity in SLE mice. While our MLD was targeted to the left ear and draining left auricular lymph node, reduced inflammation at the site of greatest UVR exposure (left ear versus the fur-covered back, for example) and its draining lymph node could potentially have a systemic effect, as soluble mediators including antigen and inflammatory cytokines can travel from the skin to draining lymph node and then, via efferent flow from the lymph node, out to the systemic circulation to the spleen and end organs (12). Also, reduced B and T cell responses in the draining lymph node would lead to fewer cells and autoantibodies leaving the lymph node to reach the circulation and spleen and other tissues to carry out inflammatory, effector, or memory functions. Furthermore, some inflammatory cells can also leave the skin directly into the blood circulation by reverse transmigration from tissue into blood vessels, as has been shown for neutrophils in UVR-treated skin (44).

We thus asked whether improving lymphatic flow in the LEC^{PTEN}-IMQ mice or by local MLD can affect parameters of systemic disease activity. We first looked at the splenomegaly that characterizes both the IMQ and LPR models (37, 45). Spleens do not have afferent lymphatics (46), and so splenic changes are considered to reflect systemic changes. LEC^{PTEN}-IMQ mice had reduced splenic weight compared with LEC^{WT}-IMQ mice (Figure 4A), suggesting reduction in systemic disease activity with improved lymphatic flow. To determine whether MLD could also affect systemic disease activity, we treated LPR mice with MLD for 4–5 weeks, a duration that would allow indirect splenic changes to occur and for turnover of pre-MLD autoantibodies (47). MLD-treated LPR mice showed reduced splenic weight compared with mice that did not receive MLD, suggesting that longer term MLD can reduce systemic disease (Figure 4B). We further measured levels of serum autoantibodies after 4–5 weeks of UVR with and without MLD. While high-titer anti-DNA and ribonucleoprotein (RNP) antibodies remained unchanged, antibodies against complement pathway components (C5, C9, factor B, factor I, factor P), histone 2B, and β2 glycoprotein were reduced (Figure 4, C and D). Interestingly, LPR mice also expressed autoantibodies found in dermatomyositis patients (TIF1γ, Jo1, PL-7, SAE1/SAE2, MDA5, NXP2, mi-2, PM/Scl100) who also demonstrate photosensitivity (48), and some of these (Jo-1,NXP2, PM/Scl100) were also reduced with MLD (Figure 4, C and D). The reduced splenomegaly and autoantibody levels suggest that longer term MLD can reduce systemic disease activity.

Improving lymphatic flow increases lymph node FRC CCL2, monocyte ROS generation, and restrains plasmablast responses in a monocyte-dependent manner. To understand how improving lymphatic flow limits lymph node B cell responses, we considered that FRCs are among the initial sensors of lymph fluid within lymph nodes and asked whether improving lymphatic flow could drive an FRC-monocyte axis that we have previously shown to regulate plasmablast accumulation in healthy mice (28). In this axis, stromal CCL2 in the T zone and the medulla induced local $CCR2^+Ly6^{hi}$ monocytes to upregulate ROS expression, which then limited survival of plasmablasts that were colocalized with the CCL2-expressing FRCs and monocytes. Upon MLD of IMQ-treated CCL2-GFP reporter mice, FRCs in the draining auricular lymph nodes showed upregulated GFP, suggestive of upregulated CCL2 expression (Figure 5A). By anti-CCL2 staining, an increase in FRC CCL2 was also detectable in LEC^{PTEN}-IMQ mice compared with control LEC^{WT}-IMQ mice (Figure 5B). Additionally, MLD also increased FRC numbers (Figure 5C), which likely reflected the increased proliferation rate, as indicated by increased Ki-67 levels (Figure 5, D and E). This expansion of FRC numbers likely added further to the level of CCL2 sensed by $CCR2^+$ cells in the lymph node. Together, our results suggested that improving lymphatic flow increased the level of FRC CCL2 in draining lymph nodes.

In association with the stromal CCL2 upregulation, $Ly6C^{hi}$ monocyte numbers were unchanged (Figure 5F), but monocyte ROS expression was increased (Figure 5G). The monocyte ROS increase was specific to this population, as B cells did not show a similar

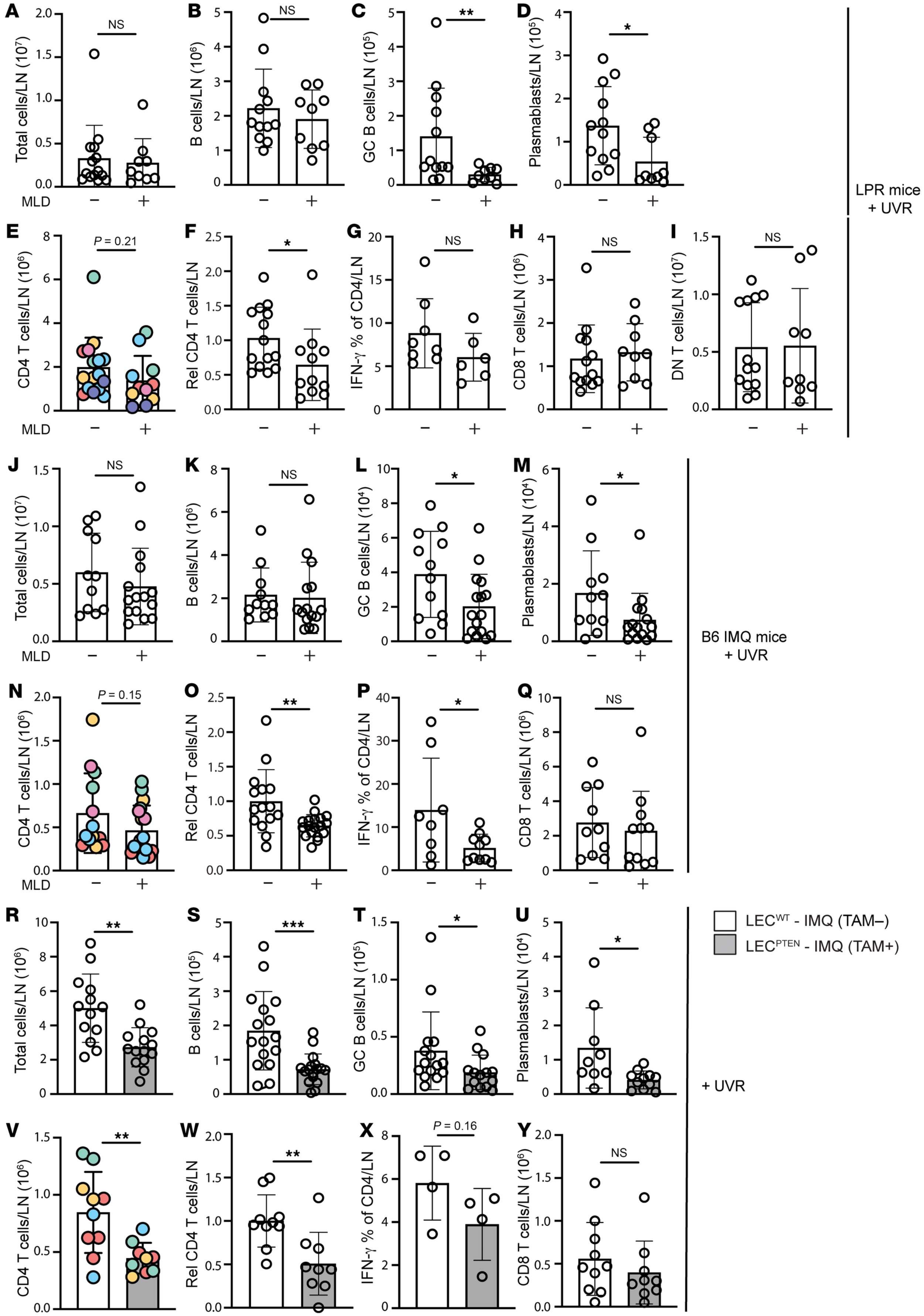
A
Total cells/LN (10^7)
2.0
1.5
1.0
0.5
0.0
NS
MLD
–
+
B
B cells/LN (10^6)
5
4
3
2
1
0
NS
–
+
C
GC B cells/LN (10^5)
5
4
3
2
1
0
**
–
+
D
Plasmablasts/LN (10^5)
4
3
2
1
0
*
–
+
LPR mice
+ UVR
E
CD4 T cells/LN (10^6)
8
6
4
2
0
P = 0.21
MLD
–
+
F
Rel CD4 T cells/LN
2.5
2.0
1.5
1.0
0.5
0.0
*
–
+
G
IFN-γ % of CD4/LN
20
15
10
5
0
NS
–
+
H
CD8 T cells/LN (10^6)
4
3
2
1
0
NS
–
+
I
DN T cells/LN (10^7)
1.5
1.0
0.5
0.0
NS
–
+
J
Total cells/LN (10^7)
1.5
1.0
0.5
0.0
NS
MLD
–
+
K
B cells/LN (10^6)
8
6
4
2
0
NS
–
+
L
GC B cells/LN (10^4)
10
8
6
4
2
0
*
–
+
M
Plasmablasts/LN (10^4)
6
4
2
0
*
–
+
B6 IMQ mice
+ UVR
N
CD4 T cells/LN (10^6)
2.0
1.5
1.0
0.5
0.0
P = 0.15
MLD
–
+
O
Rel CD4 T cells/LN
2.5
2.0
1.5
1.0
0.5
0.0
**
–
+
P
IFN-γ % of CD4/LN
40
30
20
10
0
*
–
+
Q
CD8 T cells/LN (10^6)
10
8
6
4
2
0
NS
–
+
R
Total cells/LN (10^6)
10
8
6
4
2
0
**
S
B cells/LN (10^5)
5
4
3
2
1
0
***
T
GC B cells/LN (10^5)
1.5
1.0
0.5
0.0
*
U
Plasmablasts/LN (10^4)
5
4
3
2
1
0
*
☐ LEC^WT - IMQ (TAM–)
▨ LEC^PTEN - IMQ (TAM+)
+ UVR
V
CD4 T cells/LN (10^6)
1.5
1.0
0.5
0.0
**
W
Rel CD4 T cells/LN
2.0
1.5
1.0
0.5
0.0
**
X
IFN-γ % of CD4/LN
8
6
4
2
0
P = 0.16
Y
CD8 T cells/LN (10^6)
2.0
1.5
1.0
0.5
0.0
NS

Figure 3. Improving lymphatic flow reduces draining lymph node B and T cell responses in SLE models. (**A**–**Q**) Left auricular lymph nodes of (**A**–**I**) LPR, (**J**–**Q**) B6-IMQ, and (**R**–**X**) LEC^{PTEN}-IMQ and LEC^{WT}- IMQ mice that were treated as in Figure 2A, K, and Q were examined. (**A**, **J**, and **R**) Lymph node cellularity. (**B**, **K**, and **S**) B cell, (**C**, **L**, and **T**) germinal center (GC) B cell, (**D**, **M**, and **U**) plasmablast, and (**E**, **N**, and **V**) TCR $CD4^+$ T cell numbers. (**F**, **O**, and **W**) $CD4^+$ T cell numbers normalized to control. Rel, relative. (**G**, **P**, and **X**) Percentage of $CD4^+$ T cells that express IFN-γ. (**H**, **Q**, and **Y**) $CD8^+$ and (**I**) DN T cell numbers. Each symbol represents 1 mouse; $n = 4$ to 17 per condition; data are from 2 (**X**), 3 (**G**, **P**, and **Q**), 4 (**A**–**C**, **H**–**K**, **M**, **V**, **W**, and **Y**), 5 (**D**, **N**, and **O**), 6 (**E**, **F**, **L**, **R**, and **U**), and 8 (**S** and **T**) independent experiments. Normality was assessed using the Shapiro-Wilk test. If normal, unpaired *t* test was used. If data were not normal, Mann-Whitney *U* test was used. $^{***}P < 0.001$; $^{**}P < 0.01$; $^{*}P < 0.05$. Error bars represent SD.

increase (Figure 5G). This finding of unchanged monocyte numbers but upregulated ROS expression was consistent with the FRC-monocyte axis in healthy mice (28). Together, these results were consistent with a model whereby improving lymphatic flow increased stromal CCL2, which then increased $CCR2^+Ly6C^{hi}$ monocyte expression of ROS to control B cell responses in draining lymph nodes.

To test this model, we took 2 approaches to ask the extent to which monocytes were required for the reduced B cell responses seen with improved lymphatic flow. We used anti–Gr-1 (28), which depleted both monocytes (Figure 5, H–J) and neutrophils (Supplemental Figure 6A) in B6-IMQ mice during UVR and MLD. This depletion was associated with restoration of germinal center B cell and plasmablast numbers to the higher levels seen in mice without MLD (Figure 5, K and L; compare with Figure 3, L and M), suggesting that MLD-driven reduction in B cell responses was dependent on myeloid cells. To further assess the role of monocytes without depleting neutrophils, we induced the IMQ model in CCR2-DTR mice, injected diphtheria toxin (DT) to deplete monocytes (Figure 5, M–O) but not neutrophils (Supplemental Figure 6B), and then treated with UVR and MLD (Figure 5M). Germinal center B cell numbers were not altered, but plasmablast numbers were restored to the higher levels seen in mice without MLD (Figure 5, P and Q; compare with Figure 3, L and M). The results of the Gr-1 depletion and the CCR2-DTR model together suggested that improved lymphatic flow limits plasmablast accumulation in a monocyte-dependent manner, while the reduction in germinal center B cells is mediated by other mechanisms. Altogether, our data suggested a model whereby restoring lymphatic flow in UVR-treated SLE mice reduces draining lymph node B cell responses at least in part by upregulating stromal CCL2 and increasing monocyte ROS to limit plasmablast accumulation.

Discussion

Lymphatic flow is critical for clearing inflammatory mediators from peripheral tissues and communicating with draining lymph nodes, and our results suggested that the link between UVR-induced photosensitive skin responses and increased autoimmunity in SLE is at least in part due to a propensity for SLE skin to develop UVR-induced lymphatic dysfunction. By correcting this dysfunction using either MLD or a transgenic model with increased lymphatic flow, we showed that this lymphatic dysfunction contributed to both upstream cutaneous photosensitive responses and downstream draining lymph node B and T cell responses. While the contribution of lymphatic dysfunction to increasing skin inflammation is consistent with findings in nonlupus models (42, 49), we establish here that lymphatic dysfunction also contributes to B and T cell responses in lymph nodes. Our results suggest that lymphatic dysfunction prevents optimal function of the regulatory FRC/monocyte axis in lymph nodes that normally limits plasmablast responses and that improving lymphatic function and reducing B cell responses, over the long term, can reduce autoantibody titers. Reduced antibody titers, in turn, have the potential to lead to reduced deposition of immune complexes and limit inflammation and damage in skin, kidneys, and other end organs. Together, our results suggested that UVR-induced lymphatic flow dysfunction is a contributing factor to lupus pathophysiology and points to lymphatic modulation of lymph node stromal function as a therapeutic target for UVR-induced disease flares.

Our finding that lymphatic flow modulates the lymph node stromal phenotype in SLE models underscores the importance of the communication between tissue and lymph nodes and highlights FRC regulation as an outcome of this communication. In this setting, FRCs act as a rheostat that senses and converts peripheral tissue signals into regulators of lymph node activity. We showed that improving flow was connected functionally to the FRC CCL2/monocyte ROS axis that we had previously delineated in the setting of immune responses in nonlupus models. Consistent with the findings in healthy mice, this axis contributed to limiting plasmablast responses and not germinal center responses. Anatomically, CCL2 FRCs are positioned with plasmablasts within the T cell zone and medulla, where they are able to modulate local monocytes, and consequently the plasmablasts (28, 50). FRCs, similar to fibroblasts in the synovium and other tissues (51, 52), comprise multiple subsets that have distinct functions related to their anatomic positioning within lymph nodes (25, 26); it will be interesting to further understand how different FRC subsets are modulated phenotypically and functionally by changes in lymphatic flow.

The ways by which lymphatic flow modulates FRC phenotype remains to be determined. FRCs are excellent mechanosensors and respond to environmental alterations to modulate immune function (53–55), and our results may reflect FRC sensing of changes in parameters such as shear stress as lymphatic flow changes. It is also possible that our results reflect FRC sensing of different soluble mediators originating in the skin as lymphatic flow and consequent skin inflammation is modulated (56). For example, with the MLD-induced reduction of T cell IFN-γ expression in skin, there could be reduced levels of IFN that reach the lymph node FRCs, thus altering the FRC phenotype. The reduced skin inflammation could also include reduced type I IFN expression in skin, with reduced type I IFN flowing to draining lymph nodes. Here, it is interesting to note that Interferon-α/β receptor (IFNAR) deletion from FRCs has been shown to upregulate FRC CCL2 expression (57), raising the possibility that reduced type I IFN coming from the skin could cause FRC CCL2 upregulation and activate the FRC/monocyte axis to limit B cell responses. Yet another potential way by which improving lymphatic flow can modulate FRC function is that while dendritic cell mobilization from skin to lymph nodes is relatively well preserved even in the face of changes in lymphatic fluid flow (58), dendritic cells can modulate FRC phenotype (59)

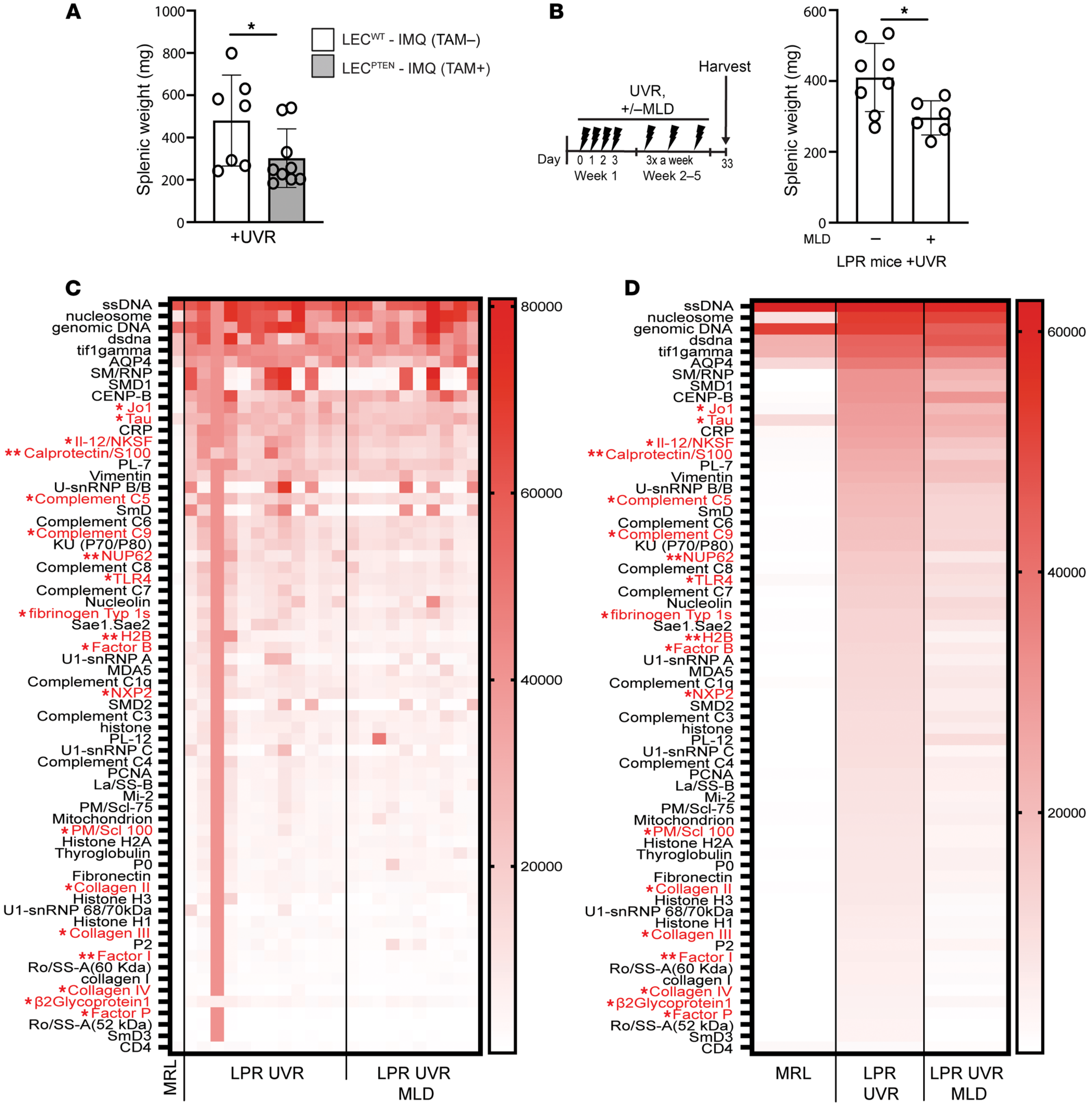

Figure 4. Improving lymphatic flow long term reduces systemic disease activity. (**A**) Splenic weight of LEC^{PTEN}-IMQ and LEC^{WT}-IMQ mice treated with UVR for 4 days. (**B**) Splenic weight of LPR mice treated with UVR and MLD concurrently or control handled for 5 weeks. (**C** and **D**) Heatmap of normalized signal intensity (NSI) from autoantigen microarray panel for IgG of MRL mice, LPR mice treated with UVR, and LPR mice treated with both UVR and MLD for 4–5 weeks. (**C**) Each column represents 1 mouse and autoantibodies with significant differences between LPR UV and LPR UV+MLD are labeled in red. (**D**) Each column represents average NSI of all mouse serum samples. Each symbol represents 1 mouse; $n = 1$ to 12 per condition; data are from 1 (**B**), 2 (**C** and **D**), and 6 (**A**) independent experiments. Normality was assessed using the Shapiro-Wilk test. If normal, unpaired t test was used. If data were not normal, Mann-Whitney U test was used. $^{**}P < 0.01$; $^{*}P < 0.05$. Error bars represent SD.

and skin dendritic cell alterations induced by the reduced skin inflammation upon improving lymphatic flow may potentially alter FRC function upon dendritic cell migration to draining nodes. Further elucidation of how lymphatic manipulation impacts the lymph node stromal compartment will be an important future direction.

The reduced lymphatic flow and relationship to B cell responses in lupus models echoes the findings of Swartz and colleagues who showed in otherwise healthy mice that a dearth of dermal lymphatics leads over time to autoantibody generation (17). Our data showing that lymphatic function is connected to a lymph node FRC/monocyte

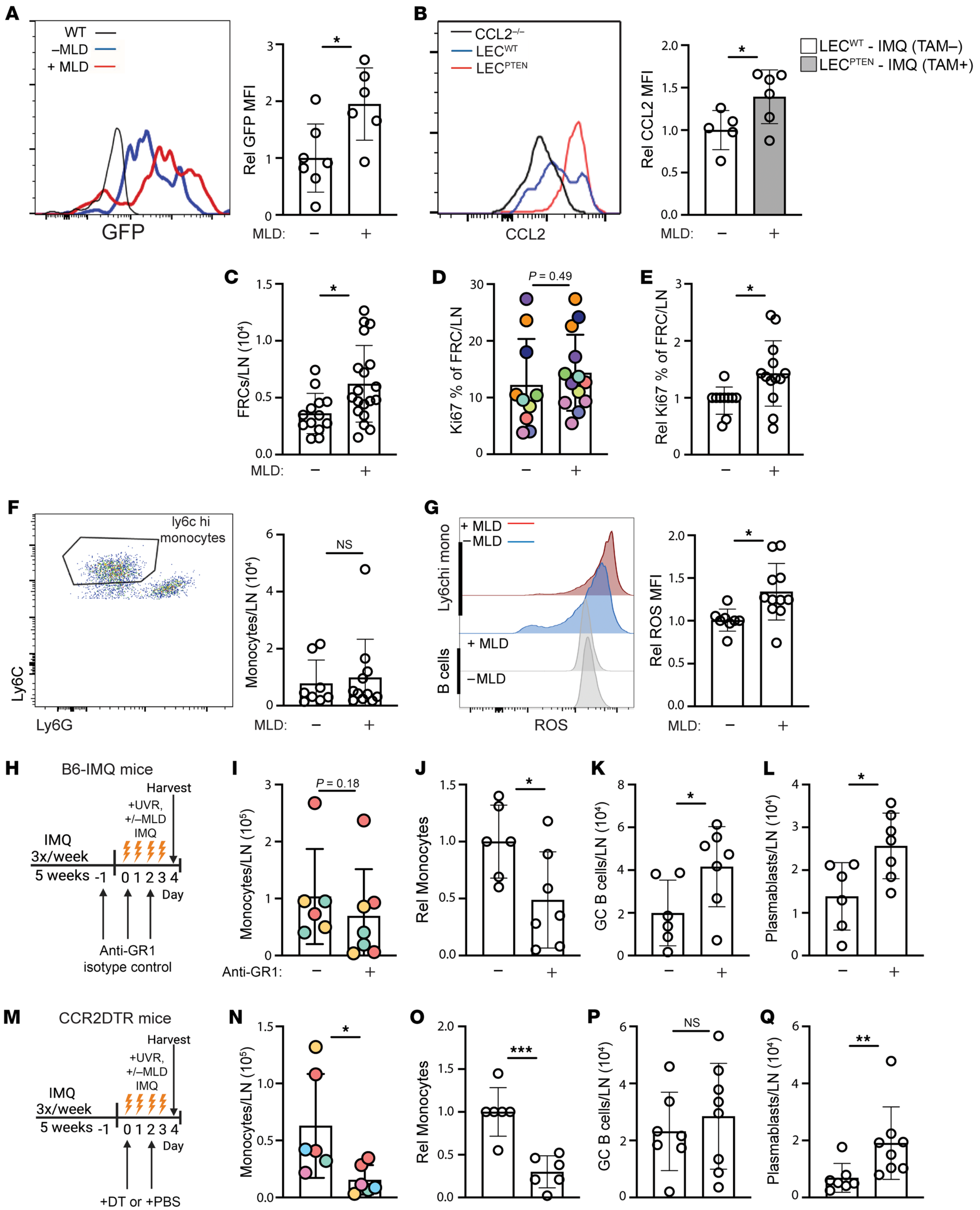
A
WT
–MLD
+ MLD
GFP
Rel GFP MFI
MLD: – +
*
B
CCL2–/–
LECWT
LECPTEN
CCL2
Rel CCL2 MFI
MLD: – +
*
LECWT - IMQ (TAM–)
LECPTEN - IMQ (TAM+)
C
FRCs/LN (10⁴)
MLD: – +
*
D
P = 0.49
Ki67 % of FRC/LN
E
Rel Ki67 % of FRC/LN
*
F
ly6c hi monocytes
Ly6C
Ly6G
Monocytes/LN (10⁴)
NS
MLD: – +
G
+ MLD
–MLD
Ly6chi mono
B cells
ROS
Rel ROS MFI
*
MLD: – +
H
B6-IMQ mice
Harvest
+UVR, +/–MLD IMQ
IMQ 3x/week
5 weeks -1 0 1 2 3 4 Day
Anti-GR1 isotype control
I
P = 0.18
Monocytes/LN (10⁵)
Anti-GR1: – +
J
Rel Monocytes
*
K
GC B cells/LN (10⁴)
*
L
Plasmablasts/LN (10⁴)
*
M
CCR2DTR mice
Harvest
+UVR, +/–MLD IMQ
IMQ 3x/week
5 weeks -1 0 1 2 3 4 Day
+DT or +PBS
N
Monocytes/LN (10⁵)
*
DT: – +
O
Rel Monocytes
***
P
GC B cells/LN (10⁴)
NS
Q
Plasmablasts/LN (10⁴)
**

Figure 5. Improving lymphatic flow increases lymph node FRC proliferation, FRC CCL2, monocyte ROS generation, and limits plasmablast numbers in a monocyte-dependent manner. (**A**–**Q**) Left auricular lymph nodes of indicated mice exposed to 4 days of UVR were examined. (**A**) FRC expression of GFP in CCL2-GFP reporter mice treated with IMQ that received MLD or control handling with UVR. (**B**) CCL2 expression by FRCs in LEC^{PTEN}-IMQ and LEC^{WT}- IMQ mice. (**A** and **B**) Representative histograms (left) and graphs (right). MFI, geometric mean fluorescence intensity. (**C**–**G**) B6-IMQ mice received 4 days of +/-MLD with UVR. (**C**) FRC numbers. (**D**) Percentage of FRCs that express Ki-67, (**E**) normalized to control handled mice. (**F**) Ly6C^{hi} monocyte numbers, flow cytometry gating (left), and numbers (right). (**G**) Monocyte ROS measured using CM-H2DCFDA, representative histograms (left) and relative MFI of CM-H2DCFDA (right). (**H**–**L**) B6-IMQ mice were treated with anti-Gr-1 or isotype control at days –1, 0, and +2 of UVR and MLD treatments as shown in **H**. (**I**) Monocyte numbers and (**J**) normalized to isotype control. (**K**) Germinal center B cell and (**I**) plasmablast numbers. (**M**–**Q**) CCR2-DTR mice were treated with DT at days 0 and 2 of UVR and MLD treatments as shown in **M**. (**N**) Monocyte numbers and (**O**) normalized to control. (**P**) Germinal center B cell and (**Q**) plasmablast numbers. Each symbol represents 1 mouse; n = 6 to 19 per condition; data are from 2 (**B**), 3 (**A** and **I**–**L**), 5 (**N** and **O**), 6 (**D**–**G**, **P**, and **Q**), and 7 (**C**) independent experiments. Normality was assessed using the Shapiro-Wilk test. If normal, unpaired t test was used. If data were not normal, Mann-Whitney U test was used. ***$P < 0.001$; **$P < 0.01$; *$P < 0.05$. Error bars represent SD.

axis that we have previously shown in healthy mice (28) to limit B cell responses provides a potential mechanism to explain these findings. This would suggest that the lymphatic regulation of the FRC/monocyte axis is a physiologic mechanism for immune regulation and that the effects of UVR exposure on autoimmunity in lupus is, in part, a disruption of this physiologic lymphatic/FRC/monocyte axis.

Our study leads to many more questions. It will be interesting to understand the other mechanisms by which lymphatic flow impacted lymph node immune function. For example, the lymphatic-modulated FRC/monocyte axis in lupus model mice contributed to limiting plasma cell responses and not germinal center responses. In LPR mice, reduced TFH numbers by improved lymphatic flow may have contributed to reduced germinal center responses; how improving lymphatic flow reduced TFH numbers or the T cell IFN-γ expression in both LPR and IMQ models in lymph nodes and the extent to which these changes are the consequence of FRC changes remains to be examined. It will also be interesting to understand the mechanisms by which lupus leads to lymphatic dysfunction. Type I IFN has been shown to inhibit dermal lymphatic fluid transport in the setting of a vaccinia skin infection model (60), suggesting the possibility that the high IFN-I tone in nonlesional human and murine lupus skin (39, 61–63) combined with UVR-induced IFN-I upregulation (64) could be contributing to the lymphatic dysfunction that we observe. The high IFN tone and other features of lupus skin may also contribute to lymphatic flow changes even without UVR exposure that was not captured with our Evans blue dye assay but that may have immune consequences. Additionally, LECs play important roles in regulating the immune cells that enter and migrate within the lymphatics (65–67); the ways in which the LEC phenotype is altered in lupus skin and the impact on autoimmunity will be interesting to understand going forward.

Our results have clinical implications. Potentially, MLD could be used in addition to current medical therapies to reduce local cutaneous inflammation or, over a larger area over time, to contribute to reducing systemic disease. Examination will be needed to assess the utility of MLD as an accessible and relatively inexpensive adjunct approach to ameliorate disease in SLE.

Methods

Sex as a biological variable. Our study examined male and female animals, and similar findings are reported for both sexes.

Study design. The purpose of this study was to examine lymphatic function in the skin of photosensitive SLE mouse models and human SLE skin and to understand the contributions of lymphatic function on cutaneous photosensitive and lymph node responses. Laboratory mice were used as subjects for experiments. Human skin sections were also analyzed. Evans blue lymphangiography was used to assess lymphatic flow, and flow cytometry was used to identify and quantify cell numbers. For experiments, sample sizes of n = 3–21 animals per condition were evaluated in 1 to 11 independent experiments.

Human samples staining and imaging. Formalin-fixed, paraffin-embedded (FFPE) sections from skin biopsies of 8 patients with SLE and/or persistently positive APL examined previously (32) were used to stain for lymphatic vessels. Patients in the study had active livedo reticularis, and staining for lymphatic vessels was done on biopsies taken from the purple areas of the livedo. Five patients had SLE, 3 of which had concomitant persistent positive APL, and 3 patients had persistent positive APL without SLE. Two archived samples from healthy donors were also used.

Five-micrometer paraffin sections were deparaffinized in xylene and rehydrated in a graded alcohol series. After a final wash with distilled water, specimen slides were placed in boiling Antigen Unmasking Solution, Tris-Based (Vector Laboratories) for 15 minutes. Slides were briefly washed in water and thereafter in PBS–0.025% Triton X-100 prior to blocking nonspecific binding sites with PBS-3% BSA for 30 minutes at room temperature. Double immunostaining was performed with 1:40 dilution in PBS/0.5% BSA of anti-podoplanin (PDPN) (D2-40, BioLegend) and 1:100 dilution of anti-CD31/PECAM-1 (Novus Biologicals) overnight at 4°C. Slides were washed with PBS-0.025% Triton X-100, and endogenous peroxidase was inhibited by incubating slides in 3% H_2O_2 for 15 minutes in the dark. The sections were then washed in distilled water followed by wash buffer and incubated with alkaline phosphatase–conjugated donkey anti-mouse (catalog 715-56-151) and horseradish peroxidase–conjugated donkey anti-rabbit secondary antibodies (catalog 711-036-152) (both Jackson ImmunoResearch) at 1:100 dilution (prepared in tris-buffered saline [TBS] with 0.5% BSA) for 1 hour at room temperature. The reaction was revealed with a 3,3′-Diaminobenzidine Substrate Kit for peroxidase and fast blue substrate (both Sigma-Aldrich) for alkaline phosphatase. At the end of incubation, slides were washed in TBS-0.025% Triton X-100, mounted with Clear-Mount (Electron Microscopy Sciences), and baked at 56°C for 20 minutes. Imaging was performed with Leica Aperio CS2 slide scanner at ×40 magnification and ImageJ (NIH) analysis software used to measure the lumenal area of PDPN$^+$CD31$^+$ lymphatic vessels. Image analysis was performed blinded to the patient diagnosis.

Mice. Mice between 6 and 15 weeks of age were used unless otherwise specified. Both male and female mice were used for experiments. All experiments were performed with age- and sex-matched controls. C57BL/6, CCL2$^{-/-}$ (68), CCL2-GFP (69), MRL, and LPR mice were originally from Jackson Laboratory and bred at our facility. PTEN$^{fl/fl}$ CreERT2 (42) were as described. CCR2-DTR (70) mice were bred at our facility.

MLD. MLD was adapted to the mouse by a licensed physical therapist with experience in MLD. MLD targeting the left ear was performed daily as specified. ProDerma smooth, powder-free latex gloves (Uniseal) were used to minimize friction and cutaneous trauma and all movements were done at a speed of 1–2 seconds per movement. Mice were anesthetized throughout procedure. The first step was the clearing step, and this started with passive motion of the left forelimb, where the mouse was placed in a supine position, held by the paw and clockwise rotations were performed (20 repetitions) to clear the supraclavicular and axillary area. Subsequently, stationary circular movements with light pressure of the index finger were applied on the left submandibular area followed by the auricular area (20 reps each). The mouse was then placed in the right lateral decubitus position to proceed with the reabsorption step which was performed in a specific sequence: (a) The left ear was held gently with a pincer grip (thumb and index finger), and light sweeping movements with the index finger were done on the ventral surface of the ear from distal to proximal (50 reps); (b). Placed in a prone position, the ear was gently held with a pincer grip and sweeping movements were done from distal to proximal on the dorsum of the base of the ear (where the large collecting lymphatic vessels are and can be visualized by Evan's blue lymphangiography) (200 reps); (c). Placed back to the right lateral decubitus position, sweeping movements at the base of the ear toward the auricular lymph node were performed (20 reps); (d) Finally placed in supine position again, the same clockwise rotations of the left forelimb were performed (20 reps). Handling controls were anesthetized in the same manner as for MLD, and the mouse was placed prone and left ear was held with a pincer grip similarly to MLD for 5 minutes.

Mouse treatments. For UVR treatments, mice were exposed to 1000–1500 J UVB/m^2/day for 4 consecutive days using a bank of 4 FS40T12 sunlamps, as previously described (35). For long-term treatment, mice were exposed to UVR for 4 consecutive days the first week and then for 3 consecutive days/week in the following weeks. To measure ear swelling after UVR exposure, a caliper (Mitutoyo) was used. Each ear was measured in the anterior half of the ear 3 times, and the average was taken.

For the IMQ-induced lupus mouse model, mice were painted on the dorsal and ventral sides of the right ear with 5% IMQ cream (Taro Pharmaceutical) 3×/week for 4–5 weeks (~50 mg/mouse total cumulative dose) (37).

For mice receiving tamoxifen, tamoxifen (Sigma-Aldrich) in corn oil was injected i.p. at a dose of 300 mg/kg/d every other day for 3 doses.

For monocyte depletion studies in the B6-IMQ mice, anti-Gr1 (RB6-8C5) or isotype control IgG (LTF-2) (both BioXCell, Lebanon, NH) were injected i.p. at a dose of 250 μg in 200 μl PBS on indicated days. To deplete monocytes in the CCR2-DTR mice, diphtheria toxin (Enzo Life Sciences) was injected i.p. at a dose of 250 ng in 200 μL PBS.

Evans blue lymphatic function assay. Evans blue retention assay was performed as previously described (71). Mouse ears were injected intradermally at the tip using a Hamilton syringe (1701, 10 μL syringe) with a 30-gauge needle; 1 μL of 2% Evans blue (Sigma-Aldrich) was injected and mice were euthanized 22–24 hours later. The harvested ear was placed in 300 μL formamide at 58°C overnight to extract Evans blue, which was quantified by absorbance with a Multiskan Ascent plate reader (Titertek) at 620 nm using a titration curve.

ROS staining. Intracellular ROS was measured using 5-(and6) chloromethyl-2′,7′-dichlorodihydrofluorescein diacetate, acetyl ester (CM-H2DCFDA, Thermo Fisher Scientific), as described previously (28). The dye was reconstituted at 5 mmol/L in DMSO and stored at –20°C. Cells were prepared in RPMI and stained with 1/500 dilution of the stock in PBS for 30 minutes at 37°C prior to flow cytometric analysis.

Flow cytometry staining and quantification. For flow cytometric staining of skin, single-cell suspensions were generated as previously described (72). In brief, ears were finely minced, digested in type II collagenase (616 U/mL; Worthington Biochemical Corporation), dispase (2.42 U/mL; Life Technologies), and DNAse1 (80 μg/mL; Sigma-Aldrich), incubated at 37°C while shaking at 100 rpm, triturated with glass pipettes, and filtered.

For staining of lymph node cells, hematopoietic cells from lymph nodes were obtained by mashing the lymph nodes and extruding the cells through a 70 μm strainer. Stromal cells were obtained as previously described (73); lymph nodes were minced, digested with type II collagenase (616 U/mL) and DNAase1 (40 μg/mL) at 37°C while shaking at 50 rpm, triturated with glass pipettes, and filtered.

To count cells, the single-cell suspension from the whole lymph node or ear was washed and resuspended in 300 μL of buffer; 10 μL was taken to be counted on the Multisizer 4e Coulter Counter (Beckman Coulter), and this count was used to calculate total number of cells per lymph node. One to two million cells per sample were stained, and most of the sample was run on the flow cytometer. To obtain absolute numbers of a particular population of cells per ear or lymph node, the frequency of these cells (of the total) in the FACS analysis was multiplied by the total number of cells per tissue (as calculated by the Multisizer 4e Coulter Counter; https://www.beckman.com/cell-counters-and-analyzers/multisizer-4e).

For flow cytometry analysis, gating of specific populations was performed after excluding debris, doublets, and dead cells using DAPI (Invitrogen) for nonfixed cells. Antibodies are from BioLegend unless otherwise specified. Samples were treated with anti-mouse CD16/32 (Fc block, clone 93) prior to staining with additional antibodies. Gating strategies and antibodies used are as follows: B cells: CD45$^+$ (30-F11) B220$^+$ (RA3-6132); monocytes: CD45$^+$, B220$^–$, CD3$^–$ (145-2C11), CD11b$^+$ (M1/70), Ly6C^{hi} (HK1.4), Ly6G$^–$ (1A8); neutrophils: CD45$^+$, CD11b$^+$, Ly6C^{med}, Ly6G$^+$; germinal center B cells: CD3$^–$, B220$^+$, GL7$^+$ (GL7), PNA$^+$ (Vector Laboratories); plasmablasts: CD3$^–$, B220med-lo, CD138$^+$ (281-2). In digested tissues, plasmablasts were identified by either intracellular IgG (IgG1-A85-1, IgG2a/b-R2-40, IgG3-R40-82, all BD Biosciences) or intracellular Igκ$^+$ (187.1) (Southern Biotech) using BD Cytofix/Cytoperm kit (BD Biosciences) in lieu of CD138. Plasmablasts were confirmed by Ki-67 (16A8) staining. The following antibodies were also used: LECs: CD45$^–$, CD31$^+$ (390), PDPN$^+$ (8.1.1); blood endothelial cells: CD45$^–$CD31$^–$, PDPN$^–$; FRCs: CD45$^–$, CD31$^–$, PDPN$^+$; CD4$^+$ T cells: CD45$^+$CD4$^+$TCR-αβ$^+$ (H57-597); Tregs: TCR-αβ$^+$, CD4$^+$, CD25$^+$ (PC61), intracellular Foxp3$^+$ (FJK-16s); follicular helper T cells: TCR-αβ$^+$, CD4$^+$, CXCR5$^+$ (L138D7), PD1$^+$ (29F.1A12); Th1 cells: TCR-αβ$^+$, CD4$^+$, Foxp3$^–$, CXCR5$^–$, intracellular IFN-γ$^+$ (XMG1.2, eBioscience); and Th17 cells: TCR-αβ$^+$, CD4$^+$, Foxp3$^–$, CXCR5$^–$, intracellular IL-17$^+$ (TC11-18H10, BD Biosciences). The intracellular stains for the CD4$^+$ T cell subset were done after fixing cells with the eBioscience Intracellular Fixation & Permeabilization Buffer Set (catalog 88-8824-00). For Th1 and Th17 cells, staining was done after cells were stimulated with Cell Activation Cocktail with Brefeldin A (BioLegend, catalog 423304) in a 37°C incubator for 4 hours. CCL2 was identified by either using CCL2-GFP reporter mice or by staining. Staining for CCL2 was performed using CCL2-FITC (2H5, Invitrogen), and signal was amplified by staining with anti–FITC-biotin (1F8-1E4, Jackson ImmunoResearch) and subsequently streptavidin-FITC (Invitrogen). A negative control for GFP signal was done by using nontransgenic mice in CCL2-GFP mouse experiments. CCL2$^{-/-}$ mice were used as negative control for staining experiments.

For a detailed list of all used antibodies, refer to Supplemental Table 1.

For flow cytometry analysis, cells were analyzed using a FACSCanto or FACSSymphony (BD Biosciences) and FlowJo Software (v10.10) (Tree Star).

Cell sorting. For quantitative PCR (qPCR) of skin cell populations, cells from ear skin were pooled and then sorted using a BD Influx (BD Biosciences). LECs were selected as DAPI$^-$CD45$^-$PDPN$^+$CD31$^+$ cells. BECs were selected as DAPI$^-$CD45$^-$PDPN$^-$CD31$^+$ cells. Fibroblasts were selected as DAPI$^-$CD45$^-$PDPN$^+$CD31$^-$ cells. Macrophages were selected as DAPI$^-$CD45$^+$CD11b$^+$F4/80$^+$ cells.

RNA extraction. RNA was extracted from sorted cells using an RNAEasy Plus Kit (QIAGEN) and quality confirmed on a BioAnalyzer 2100 (Agilent Technologies).

Real time PCR. cDNA was synthesized (iScript kit, Bio-Rad) from extracted RNA and real-time PCR (iQ SYBR-Green Supermix kit, Bio-Rad) was performed using primers for PTEN (Mm_Pten_1_SG QuantiTect Primer Assay, QIAGEN) and GAPDH (R: TTGAAGTCGCAGGAGACAACCT, F: ATGTGTCCGTCGTGGATCTGA).

Autoantigen microarray. Blood was collected from mice, left at room temperature for 1 hour, and then centrifuged at 1932 *g* for 3 minutes. The supernatant containing the serum was then collected and frozen at –80°C until ready to be shipped for autoantigen microarray profiling at the Genomics and Microarray Core Facility, University of Texas Southwestern Medical Center, Dallas, Texas, USA.

Statistics. For figures showing normalized values, each individual replicate experiment was normalized for that experiment. For experiments that contained more than 1 control sample, the mean was obtained for the control samples, and the individual control and experimental samples were divided by this mean value to normalize to the control mean. The Shapiro-Wilk test was used to test for normality. Unpaired, 2-tailed *t* test was used for normal data and Mann-Whitney *U* test was used otherwise.

Study approval. All animal experiments and research plans were approved by the Institutional Animal Care and Use Committee at Weill Cornell Medicine. Ethical approval for human studies was obtained from the Hospital for Special Surgery Institutional Review Board (IRB number: 2015-256), where participants had signed written, informed consents for both the initial study and for the subsequent study of skin biopsies.

Data availability. The murine RNA-Seq data have been previously published and are publicly available in the NCBI's Gene Expression Omnibus database (GEO GSE255519 for IMQ mice) (39). Values for all data points in graphs are reported in the Supporting Data Values file.

Author contributions

WGA, NS, and TTL conceived the study. MJH, WGA, and TTL designed the study. MJH, WGA, MLSC, AR, ESS, JHS, JS, NS, WDS, DCD, CBC, RPK, and YC designed and performed the experiments and analyzed the data. ES, DE, SS, RPK, and BJM provided key reagents and intellectual input. CBC and SAR designed experiments and provided intellectual input. TTL designed, supervised, and interpreted experiments. MJH, WGA, and TTL wrote the manuscript; all authors contributed to critical reading and editing. MJH is first of the first authors because she completed the study and manuscript. WGA is the second of the first authors because he began the study and wrote the initial manuscript.

Acknowledgments

The authors thank the Lu Lab for critical reading of the manuscript. This work was supported by R01AI079178-121S1 (to MJH), NIH T32AR071302-01 to the Hospital for Special Surgery Research Institute Rheumatology Training Program (to NS and WDS), NIH MSTP T32GM007739 to the Weill Cornell/Rockefeller/Sloan-Kettering Tri-Institutional MD-PhD Program (to WDS), the Emerson Collective Cancer Research Fund 691032 (to RPK), NIH R01AI079178 (to TTL), R01AR084694 (to TTL), R21 AR081493 (to TTL), DOD W81XWH-22-1-0627 (to TTL), the Lupus Research Alliance (to TTL), the St. Giles Foundation (to TTL); and the NIH Office of the Director grant S10OD019986 to the Hospital for Special Surgery. Schematics in figures were created in BioRender. Lu, T. (2025) https://BioRender.com/8ksl0q5.

Address correspondence to: Theresa T. Lu, Hospital for Special Surgery, 535 East 70th Street, New York, New York 10021, USA. Phone: 212.774.2532; Email: lut@hss.edu.

WGA and ES's present address is: Systemic Autoimmunity Branch, NIAMS/NIH, Bethesda, Maryland, USA.

MLSC's present address is: NJ Bio; Princeton, New Jersey, USA.

ESS's present address is: Graduate Program in Bioscience, Rockefeller University; New York, New York, USA

NS's present address is: Department of Medicine (Rheumatology), Albert Einstein College of Medicine/Montefiore Medical Center; Bronx, New York, USA

WDS's present address is: Department of Dermatology, Yale University; New Haven, Connecticut, USA

DCD's present address is: Department of Cancer Immunology, Genentech; South San Francisco, California, USA

SS's present address is: Nemours Hospital for Children, Wilmington, Delaware, USA.

---

1. Tsokos GC, et al. New insights into the immunopathogenesis of systemic lupus erythematosus. *Nat Rev Rheumatol*. 2016;12(12):716–730.
2. Stannard JN, Kahlenberg JM. Cutaneous lupus erythematosus: updates on pathogenesis and associations with systemic lupus. *Curr Opin Rheumatol*. 2016;28(5):453–459.
3. Schmidt E, et al. Sun-induced life-threatening lupus nephritis. *Ann N Y Acad Sci*. 2007;1108:35–40.
4. Foering K, et al. Characterization of clinical photosensitivity in cutaneous lupus erythematosus. *J Am Acad Dermatol*. 2013;69(2):205–213.
5. Ansel JC, et al. Effects of UV radiation on autoimmune strains of mice: increased mortality and accelerated autoimmunity in BXSB male mice. *J Invest Dermatol*. 1985;85(3):181–186.
6. Ahluwalia J, Marsch A. Photosensitivity and photoprotection in patients with lupus erythematosus. *Lupus*. 2019;28(6):697–702.
7. Kuhn A, et al. Photoprotective effects of a broad-spectrum sunscreen in ultraviolet-induced

cutaneous lupus erythematosus: a randomized, vehicle-controlled, double-blind study. *J Am Acad Dermatol*. 2011;64(1):37–48.

8. Vilá LM, et al. Association of sunlight exposure and photoprotection measures with clinical outcome in systemic lupus erythematosus. *P R Health Sci J*. 1999;18(2):89–94.
9. Mikita N, et al. Recent advances in cytokines in cutaneous and systemic lupus erythematosus. *J Dermatol*. 2011;38(9):839–849.
10. Ogunsanya ME, et al. A systematic review of patient-reported outcomes in patients with cutaneous lupus erythematosus. *Br J Dermatol*. 2017;176(1):52–61.
11. Tebbe B, Orfanos CE. Epidemiology and socioeconomic impact of skin disease in lupus erythematosus. *Lupus*. 1997;6(2):96–104.
12. Sim JH, et al. Immune cell-stromal circuitry in lupus photosensitivity. *J Immunol*. 2021;206(2):302–309.
13. Kahlenberg JM. Rethinking the pathogenesis of cutaneous lupus. *J Invest Dermatol*. 2021;141(1):32–35.
14. Patel J, et al. An update on the pathogenesis of cutaneous lupus erythematosus and its role in clinical practice. *Curr Rheumatol Rep*. 2020;22(10):69.
15. Oliver G, et al. The lymphatic vasculature in the 21st Century: novel functional roles in homeostasis and disease. *Cell*. 2020;182(2):270–296.
16. Fonseca DM, et al. Microbiota-dependent sequelae of acute infection compromise tissue-specific immunity. *Cell*. 2015;163(2):354–366.
17. Thomas SN, et al. Impaired humoral immunity and tolerance in K14-VEGFR-3-Ig mice that lack dermal lymphatic drainage. *J Immunol*. 2012;189(5):2181–2190.
18. Kajiya K, Detmar M. An important role of lymphatic vessels in the control of UVB-induced edema formation and inflammation. *J Invest Dermatol*. 2006;126(4):919–921.
19. Rajasekhar L, et al. Lymphatic obstruction as a cause of extremity edema in systemic lupus erythematosus. *Clin Rheumatol*. 2013; 32(Suppl 1):S11–S13.
20. Daniel A, et al. Chylous ascites in a patient with an overlap syndrome: a surprising response to rituximab. *BMJ Case Rep*. 2017;2017:bcr2017222339bcr-2017-222339.
21. Dalvi SR, et al. Pseudo-pseudo Meigs' syndrome in a patient with systemic lupus erythematosus. *Lupus*. 2012;21(13):1463–1466.
22. Lee CK, et al. Concurrent occurrence of chylothorax, chylous ascites, and protein-losing enteropathy in systemic lupus erythematosus. *J Rheumatol*. 2002;29(6):1330–1333.
23. Ulvmar MH, et al. The atypical chemokine receptor CCRL1 shapes functional CCL21 gradients in lymph nodes. *Nat Immunol*. 2014;15(7):623–630.
24. Gretz JE, et al. Lymph-borne chemokines and other low molecular weight molecules reach high endothelial venules via specialized conduits while a functional barrier limits access to the lymphocyte microenvironments in lymph node cortex. *J Exp Med*. 2000;192(10):1425–1440.
25. Li L, et al. Lymph node fibroblastic reticular cells steer immune responses. *Trends Immunol*. 2021;42(8):723–734.
26. Pikor NB, et al. Development and immunological function of lymph node stromal cells. *J Immunol*. 2021;206(2):257–263.
27. Krishnamurty AT, Turley SJ. Lymph node stromal cells: cartographers of the immune system. *Nat Immunol*. 2020;21(4):369–380.
28. Dasoveanu DC, et al. Lymph node stromal CCL2 limits antibody responses. *Sci Immunol*. 2020;5(45):eaaw0693.
29. Yazici Y, et al. Protein-losing enteropathy in systemic lupus erythematosus: report of a severe, persistent case and review of pathophysiology. *Lupus*. 2002;11(2):119–123.
30. von der Weid PY, et al. Role of the lymphatic system in the pathogenesis of Crohn's disease. *Curr Opin Gastroenterol*. 2011;27(4):335–341.
31. Rossi A, et al. Lymphatic and blood vessels in scleroderma skin, a morphometric analysis. *Hum Pathol*. 2010;41(3):366–374.
32. Sevim E, et al. Mammalian target of rapamycin pathway assessment in antiphospholipid antibody-positive patients with livedo. *J Rheumatol*. 2022;49(9):1026–1030.
33. Huggenberger R, et al. An important role of lymphatic vessel activation in limiting acute inflammation. *Blood*. 2011;117(17):4667–4678.
34. Furukawa F. Photosensitivity in cutaneous lupus erythematosus: lessons from mice and men. *J Dermatol Sci*. 2003;33(2):81–89.
35. Shipman WD, et al. A protective Langerhans cell-keratinocyte axis that is dysfunctional in photosensitivity. *Sci Transl Med*. 2018;10(454):eaap9527.
36. Menke J, et al. Sunlight triggers cutaneous lupus through a CSF-1-dependent mechanism in MRL-Fas(lpr) mice. *J Immunol*. 2008;181(10):7367–7379.
37. Yokogawa M, et al. Epicutaneous application of toll-like receptor 7 agonists leads to systemic autoimmunity in wild-type mice: a new model of systemic Lupus erythematosus. *Arthritis Rheumatol*. 2014;66(3):694–706.
38. Mizui M, et al. IL-2 protects lupus-prone mice from multiple end-organ damage by limiting CD4-CD8- IL-17-producing T cells. *J Immunol*. 2014;193(5):2168–2177.
39. Li TM, et al. The interferon-rich skin environment regulates Langerhans cell ADAM17 to promote photosensitivity in lupus. *Elife*. 2024;13:e85914.
40. Lurie F, et al. The American Venous Forum, American Vein and Lymphatic Society and the Society for Vascular Medicine expert opinion consensus on lymphedema diagnosis and treatment. *Phlebology*. 2022;37(4):252–266.
41. Lasinski BB, et al. A systematic review of the evidence for complete decongestive therapy in the treatment of lymphedema from 2004 to 2011. *PM R*. 2012;4(8):580–601.
42. Kataru RP, et al. Lymphatic-specific intracellular modulation of receptor tyrosine kinase signaling improves lymphatic growth and function. *Sci Signal*. 2021;14(695):eabc0836.
43. Schwager S, et al. Antibody-mediated delivery of VEGF-C potently reduces chronic skin inflammation. *JCI Insight*. 2018;3(23):e124850.
44. Skopelja-Gardner S, et al. Acute skin exposure to ultraviolet light triggers neutrophil-mediated kidney inflammation. *Proc Natl Acad Sci U S A*. 2021;118(3):e2019097118.
45. Liu Y, et al. Accelerated model of lupus autoimmunity and vasculopathy driven by toll-like receptor 7/9 imbalance. *Lupus Sci Med*. 2018;5(1):e000259.
46. Lewis SM, et al. Structure and function of the immune system in the spleen. *Sci Immunol*. 2019;4(33):eaau6085.
47. Vieira P, Rajewsky K. The half-lives of serum immunoglobulins in adult mice. *Eur J Immunol*. 1988;18(2):313–316.
48. Hodgkinson LM, et al. Dermatomyositis autoantibodies: how can we maximize utility? *Ann Transl Med*. 2021;9(5):433.
49. Kajiya K, et al. Activation of the VEGFR-3 pathway by VEGF-C attenuates UVB-induced edema formation and skin inflammation by promoting lymphangiogenesis. *J Invest Dermatol*. 2009;129(5):1292–1298.
50. Mohr E, et al. Dendritic cells and monocyte/macrophages that create the IL-6/APRIL-rich lymph node microenvironments where plasmablasts mature. *J Immunol*. 2009;182(4):2113–2123.
51. Smith MH, et al. Drivers of heterogeneity in synovial fibroblasts in rheumatoid arthritis. *Nat Immunol*. 2023;24(7):1200–1210.
52. Wei K, et al. Notch signalling drives synovial fibroblast identity and arthritis pathology. *Nature*. 2020;582(7811):259–264.
53. Tomei AA, et al. Fluid flow regulates stromal cell organization and CCL21 expression in a tissue-engineered lymph node microenvironment. *J Immunol*. 2009;183(7):4273–4283.
54. Horsnell HL, et al. Lymph node homeostasis and adaptation to immune challenge resolved by fibroblast network mechanics. *Nat Immunol*. 2022;23(8):1169–1182.
55. Assen FP, et al. Multitier mechanics control stromal adaptations in the swelling lymph node. *Nat Immunol*. 2022;23(8):1246–1255.
56. Howlader MJ, et al. Lymphatic messengers: Non-antigen soluble mediators from diseased tissues to draining lymph nodes. *Curr Opin Immunol*. 2025;93:102536.
57. Perez-Shibayama C, et al. Type I interferon signaling in fibroblastic reticular cells prevents exhaustive activation of antiviral CD8$^+$ T cells. *Sci Immunol*. 2020;5(51):eabb7066.
58. Platt AM, et al. Normal dendritic cell mobilization to lymph nodes under conditions of severe lymphatic hypoplasia. *J Immunol*. 2013;190(9):4608–4620.
59. Kumar V, et al. A dendritic-cell-stromal axis maintains immune responses in lymph nodes. *Immunity*. 2015;42(4):719–730.
60. Loo CP, et al. Lymphatic vessels balance viral dissemination and immune activation following cutaneous viral infection. *Cell Rep*. 2017;20(13):3176–3187.
61. Billi AC, et al. Nonlesional lupus skin contributes to inflammatory education of myeloid cells and primes for cutaneous inflammation. *Sci Transl Med*. 2022;14(642):eabn2263.
62. Der E, et al. Tubular cell and keratinocyte single-cell transcriptomics applied to lupus nephritis reveal type I IFN and fibrosis relevant pathways. *Nat Immunol*. 2019;20(7):915–927.
63. Psarras A, et al. Functionally impaired plasma-

cytoid dendritic cells and non-haematopoietic sources of type I interferon characterize human autoimmunity. *Nat Commun*. 2020;11(1):6149.

64. Skopelja-Gardner S, et al. The early local and systemic Type I interferon responses to ultraviolet B light exposure are cGAS dependent. *Sci Rep*. 2020;10(1):7908.
65. Clement CC, et al. 3-hydroxy-L-kynurenamine is an immunomodulatory biogenic amine. *Nat Commun*. 2021;12(1):4447.
66. Russo E, et al. Intralymphatic CCL21 promotes tissue egress of dendritic cells through afferent lymphatic vessels. *Cell Rep*. 2016;14(7):1723–1734.
67. Saxena V, et al. Treg tissue stability depends on lymphotoxin beta-receptor- and adenosine-receptor-driven lymphatic endothelial cell responses. *Cell Rep*. 2022;39(3):110727.
68. Lu B, et al. Abnormalities in monocyte recruitment and cytokine expression in monocyte chemoattractant protein 1-deficient mice. *J Exp Med*. 1998;187(4):601–608.
69. Shi C, et al. Bone marrow mesenchymal stem and progenitor cells induce monocyte emigration in response to circulating toll-like receptor ligands. *Immunity*. 2011;34(4):590–601.
70. Hohl TM, et al. Inflammatory monocytes facilitate adaptive CD4 T cell responses during respiratory fungal infection. *Cell Host Microbe*. 2009;6(5):470–481.
71. Escobedo N, et al. Restoration of lymphatic function rescues obesity in Prox1-haploinsufficient mice. *JCI Insight*. 2016;1(2):e85096.
72. Chia JJ, et al. Dendritic cells maintain dermal adipose-derived stromal cells in skin fibrosis. *J Clin Invest*. 2016;126(11):4331–4345.
73. Chyou S, et al. Coordinated regulation of lymph node vascular-stromal growth first by CD11c+ cells and then by T and B cells. *J Immunol*. 2011;187(11):5558–5567.